Chemical Engineering & Processing: Process Intensification 213 (2025) 110295

Contents lists available at ScienceDirect

Chemical Engineering and Processing - Process Intensification

journal homepage: www.elsevier.com/locate/cep

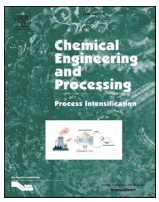

Axial dispersion modelling of the residence time distribution in a millistructured plate reactor

Lucas Schaare [a,b], Alexander Rave [a], Rafael Kuwertz [b], Georg Fieg [a], Mirko Skiborowski [a,*]

[a] Hamburg University of Technology, Institute of Process Systems Engineering, Am Schwarzenberg-Campus 4, 21073, Hamburg, Germany
[b] Ehrfeld Mikrotechnik GmbH, Mikroforum Ring 1, 55234, Wendelsheim, Germany

ARTICLE INFO

Keywords:
Process intensification
Millireactor
Residence time distribution
Axial dispersion model

ABSTRACT

Micro- and millistructured reactors offer significant advantages compared to conventional batch reactors in terms of heat and mass transfer as well as process safety. Especially in case of fast and exothermic reactions, the space-time-yield of batch reactors is often limited by poor heat transfer and slow mixing. The use of millistructured reactors, such as the ART plate reactor PR37 of Ehrfeld Mikrotechnik, can overcome heat and mass transfer limitations and significantly extend applicable process windows, while providing sufficient capacity for industrial applications. Previous investigations showed that the reactor offers high heat transfer coefficients as well as short micromixing times at moderates Reynolds numbers. In order to further characterize the performance of the reactor and the possible operating window, the current work provides a thorough study of the residence time distribution on the basis of pulse experiments and a model-based evaluation of the deviation from ideal plug flow on the basis of the axial dispersion model. The results demonstrate that the reactor closely resembles the ideal plug flow even for Reynolds numbers of just about $Re \approx 100$. Due to its meandering, periodically diverging/converging process channels, the formation of secondary flow is promoted resulting in an increased cross-mixing and thus a considerably reduced axial dispersion compared straight channels. For further analysis, as well as model-based assessment and design of the reactor, a correlation for the axial dispersion coefficient is derived which is applicable for a wide process window.

1. Introduction

Climate change and the energy transition are key challenges of the chemical industry in the 21st century [1]. Process intensification is an essential lever to address these challenges by developing more sustainable, smaller, cleaner and more energy and resource efficient processes [2]. Addressing the center piece of chemical processes, micro- and millireactors offer an important technology for process intensification [3] that is considered a key technology for the transformation from batch to continuous processes for the production of fine chemical and pharmaceuticals, which can bring significant benefits under economic and ecological aspects [4]. Micro- and millistructured reactors further allow to realize novel process windows beyond the limits of conventional batch reactors [5].

Due to the high surface-to-volume ratio, micro- and millistructured reactors facilitate precise process control under nearly isothermal conditions [6], allowing operation at higher temperature, pressure, and concentration close to the physico-chemical optimum [5]. The reduced reactor hold-up volume enhances process safety by minimizing the risk of thermal runaway, while improved mass transfer due to shorter diffusion paths ensures rapid mixing [7]. Furthermore, the well-defined process conditions enable near plug-flow behaviour [8,9], eliminating transport limitations and ensuring reactions proceed according to intrinsic kinetics [10]. As a result, micro- and millistructured reactors are well suited for strongly exothermic [11] and fast, mixing-sensitive reactions [12], leading to improved selectivity, lower separation costs and reduced environmental impact [13].

In addition, the modular design of the reactors offers a straightforward scale-up from laboratory to production scale, where the continuous operation allows to achieve production capacities which can effectively match and exceed that of conventional discontinuous batch reactor [14]. The modularity provides a high degree of flexibility, which effectively allows to address market dynamics and increasingly shorter

Abbreviations: ADM, Axial dispersion model; FFT, Fast Fourier Transformation; IFFT, Inverse Fast Fourier Transformation; RTD, Residence time distribution; TIR, Temperature indication and registration.

* Corresponding author.
E-mail address: mirko.skiborowski@tuhh.de (M. Skiborowski).

https://doi.org/10.1016/j.cep.2025.110295
Received 15 November 2024; Received in revised form 24 March 2025; Accepted 28 March 2025
Available online 28 March 2025

Nomenclature

Latin letters

c	([mol/m^3]) Concentration
Dax	([m^2/s]) Axial dispersion coefficient
dh	([m]) Hydraulic diameter
E(s)	([-]) Frequency-discrete residence time distribution
E(t)	([1/s]) Density function of residence time distribution
F(t)	([1/s]) Sum function of residence time distribution
L	([m]) Length
Q	([mL/min]) Flow rate
s	([Hz]) Frequency
t	([s]) Time
$\bar{t}$	([s]) Mean residence time
u	([m/s]) Mean velocity
Rc	([m]) Curvature radius
V	([m^3]) Volume
X(s)	([-]) Time-discrete input signal
X(t)	([1/s]) Frequency-discrete input signal
Y(s)	([-]) Time-discrete output signal
Y(t)	([1/s]) Frequency-discrete output signal
z	([m]) Relative length

Greek letters

a	([-]) Aspect ratio of rectangular cross-section
θ	([-]) Dimensionless time
$\mathfrak{F}$	([-]) Fast Fourier Transformation
$\mathfrak{F}^{-1}$	([-]) Inverse Fast Fourier Transformation
m	([-]) Moments of the residence time distribution
r	([kg/m^3]) Density
t	([s]) Residence time
ϵ	([-]) Sum of square error
η	([Pa s]) Dynamic viscosity
σ	([s^2]) Variance
χ	([-]) Dimensionless Cartesian coordinate

Dimensionless quantity

De	Dean number ($De = Re\sqrt{\frac{d_h}{2r_c}}$)
Pe_{ax}	Axial Peclet number ($Pe_{ax} = \frac{u \cdot d}{D_{ax}}$)
Bo	Bodenstein number ($Bo = \frac{u \cdot L}{D_{ax}}$)
Re	Reynolds number ($Re = \frac{u \cdot d}{\nu}$)

product life cycles in the fine and pharmaceutical industries. The great potential of micro- and millistructured reactors for process intensification has already been successfully demonstrated on industrial scale. For example, Corning® Advanced-Flow™ Reactor (AFR) Technology has successfully accomplished the first use of the G5 reactor in industrial production of agrochemicals with a throughput of 10,000 tons/a. The advanced reactor enables a 100 times enhanced mixing and 1000 times improved heat transfer compared to a conventional batch reactor [15]. Additionally, the Miprowa® reactor from Ehrfeld Mikrotechnik has successfully replaced 20 conventional batch reactors in a large-scale production plant of a highly exothermic alkoxylation reaction with a production capacity of 10,000 tons/a, while reducing the reaction volume from 50 m^3 to 40 L [16].

Despite these promising results and the high potential, the industrial application remains yet limited due to the lack of standardized reactor selection criteria, operational knowledge, and systematic evaluation methods. Experts from BASF highlight the need for reference applications and reliable performance models to facilitate technology transfer and implementation [17]. Overcoming these challenges is essential to maximize the benefits of micro- and millistructured reactors and to achieve a paradigm shift from batch to flow reactor for more sustainable and safer production processes.

A crucial parameter for evaluating reactor performance is the residence time distribution (RTD), which directly influences reactant conversion and product selectivity [13,18,19]. The RTD characterizes the flow behaviour inside the reactor, determining whether fluid elements experience uniform residence times or significant variations that may negatively impact reaction control [20]. Ideally, a narrow and symmetrical RTD, close to plug-flow, is desired to improve conversion and selectivity [21,22]. Under this condition, each molecule exhibit a constant residence time, leading to homogeneous concentration and velocity profiles and allowing for precise reaction control [23]. In contrast, broad RTDs, caused by axial dispersion, result in inefficient fluid contact, leading to reduced conversion and selectivity [18]. This can inhibit reaction rates and limit the intrinsic reaction kinetics and affect process performance.

Due to the predominantly laminar flow associated with small channels, micro- and millireactors often exhibit broad RTD resulting in increased axial dispersion and limiting their suitability for many applications [24]. However, molecular diffusion and secondary flows in structured reactors can enhance radial mixing, breaking the parabolic velocity profile of the laminar flow and thus reducing the axial dispersion [25]. For example, Dean vortices, generated by centrifugal forces in curved microchannel geometries, can improve mixing and reduce axial dispersion, achieving plug flow like behavior already at relatively low Reynolds number [26]. Several studies have demonstrated that the generation of secondary flow allows micro- and millireactor to reduce axial, leading to RTDs that closely resemble ideal plug flow [21,22,24,27–31].

However, the majority of the RTD studies focus on simple coiled tube reactors at laboratory scale, which are limited in the scale-up to industrial application. Maintaining equivalent mixing and heat/mass transfer performance is the key challenge for scale-up [14]. In contrast, the present study focuses on the RTD characterization of the ART plate reactor, a millistructured reactor specifically designed for straightforward scale-up to production capacities of kilograms per hour [38]. This work aims to fill the gap in RTD characterization for scale-up relevant reactor systems, providing a deeper understanding of axial dispersion in a scalable millistructured reactor.

To enable a model-based evaluation of the ART plate reactor, process engineers require quantitative models for mass and heat transfer, mixing, and pressure drop. While previous studies have extensively characterized the hydrodynamics [32], the heat transfer [33] and the micromixing [34] of the reactor, a systematic assessment of its RTD is still lacking. The ART reactor has demonstrated high heat transfer coefficients (~5 kW/(m^{2}K)) at moderate Reynolds numbers, making it highly suitable for strongly exothermic reactions [33]. Additionally, micromixing times below 0.1 s for $Re > 150$ indicate its excellent suitability for fast, mixing-sensitive reactions [34]. Under optimal conditions, the meandering structured milli channels of the reactor enable close to ideal plug flow conditions [22,28,31]. However, it is essential to accurately characterize and quantify deviations from ideal plug flow, as these impact reaction performance, selectivity, and scale-up.

This study aims to address this gap by analysing the residence time distribution (RTD) of the ART reactor using the axial dispersion model (ADM), which quantifies deviations from plug flow [35]. Combined with the established models for heat transfer and micromixing, the characterization and modelling of the RTD, also referred to as macromixing [36], will enable a more robust reactor performance assessment, facilitating its design, scale-up and optimizations.

2. Residence time distribution

Prior to the description of the specific reactor and the applied methods, the current section first gives a brief overview about the fundamentals of the residence time distribution, as well as the experimental characterization and analysis by means of the axial dispersion model.

2.1. Characterization of the RTD

The residence time distribution characterizes the flow behavior in a reactor and is defined by the density function $E(t)$ according to Danckwerts [42]:

$$E(t) = \frac{c(t)}{\int_0^\infty c(t)dt}, \tag{1}$$

with $c(t)$ for the time-dependent concentration. The cumulative function $F(t)$ represents the fraction of fluid that has exited by time t:

$$F(t) = \int_0^t E(t)dt, \tag{2}$$

To allow comparison across different systems, the dimensionless time is introduced as $\theta = t/\tau$, with τ as the hydrodynamic residence time, enabling normalization of the RTD:

$$E(\theta) = \tau E(t), \tag{3}$$

In order to characterize the residence time distribution, the input-response technique is applied, according to [37]. Therefore, a defined disturbance signal is injected at the reactor inlet and its change is recorded as a response signal at the reactor outlet. The relationship between the input and output signals is used to derive the residence time distribution, which is equivalent to the transfer function of the system. This relationship is defined according to system theory using the convolution integral [38].

$$y(t) = \int_0^t E(t')\cdot x(t-t')\,dt' \tag{4}$$

The input signals are usually tracers injected into the fluid flow at the reactor inlet in the form of pulses, steps, periodic or even random signals [20]. The injected tracer signal propagates through the reactor and is measured as a response signal at the reactor outlet. The tracer should not affect the fluid dynamic behavior in the reactor and must therefore match the chemical and physical properties of the process medium [39].

The injection of the tracer should be implemented by approximating a defined function in order to establish a mathematical relationship between the input signal and the response signal. The most common disturbance signals are step and pulse functions [20]. In this work, impulse experiments are used to investigate the RTD. For pulse experiments, it is important to inject a high concentration of tracer in the shortest possible time. The aim is to achieve an approximation to the so-called "Dirac pulse", which is infinitely short and high with an integral of one. In practice, an ideal Dirac pulse is impossible to realize. In order to obtain a good approximation, the injection time should be as short as possible in relation to the hydrodynamic residence time of the process [40].

The signals are analyzed with the principle of system theory by assuming linearity and time invariance. Fig. 1 shows the relationship between the input (x,X) and output functions (y,Y) in the time (t) and frequency domain (s).

The input and output signals are linearly related to the residence time distribution by the convolution integral

$$E(t) = \mathfrak{F}^{-1}\left\{\frac{\mathfrak{F}\{y(t)\}}{\mathfrak{F}\{x(t)\}}\right\} \tag{5}$$

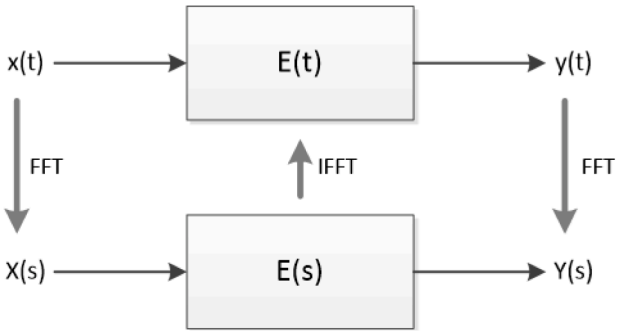

Fig. 1. System theory of the residence time distribution [41].

The Fast Fourier Transform (FFT) is used to deconvolve the integral, which requires a transformation of the signals from the time domain into the frequency domain. By transferring the functions to the frequency domain, a simple division of the input and output signal can be applied, which can be transferred back to the time-discrete domain by applying inverse Fast Fourier Transform (IFFT) [38]. In the scope of this work, Matlab is used to deconvolute the signals. In addition, filters are used to smooth the noise of the signals. The explicit procedure for signal processing using Fast Fourier Transform is described in Section 3.3.

2.2. Axial dispersion model

The experimentally determined residence time distributions are analyzed using simplified models in order to characterize the flow pattern in the reactor. Past studies have shown that the dispersion model is particularly suitable for modelling the residence time of milli and microstructured reactors [42]. The axial dispersion model is based on a strong simplification of the general convection-diffusion equation. The one-dimensional model is an extension of the ideal plug flow model taking into account real mixing effects. Within the axial dispersion model, the material balance of the transient plug flow model is extended by a disperse transport term, which is equivalent to the diffusion term of Fick's second law [43].

The corresponding differential equation is defined as follows [20]:

$$\frac{\partial c}{\partial t} = -u\frac{\partial c}{\partial z} + D_{ax}\frac{\partial^2 c}{\partial z^2} \tag{6}$$

The material balance consists of a transient term $\left(\frac{\partial c}{\partial t}\right)$, a convective transport term $\left(u\frac{\partial c}{\partial z}\right)$ and a disperse transport term $\left(D_{ax}\frac{\partial^2 c}{\partial z^2}\right)$. The disperse term includes convective mixing in the direction of flow, caused by vortex formation and turbulence, different residence times of fluid elements moving along different streamlines, caused by a non-uniform distribution of flow velocity across the channel cross-section and molecular diffusion, and is characterized by the axial dispersion coefficient D_{ax} [36]. The dispersion coefficient has the same unit as the diffusion coefficient, but is significantly larger in case of significant cross-mixing effects. The magnitude of the dispersion coefficients characterizes the deviation from an ideal plug flow. Consequently, small dispersion coefficients result in a negligible effect of the disperse term such that the differential equation approaches that of an ideal plug flow [44].

By introducing the dimensionless residence time ($\theta = t/\tau$) in Eq. (7), a dimensionless form of the differential equation is obtained

$$\frac{\partial c}{\partial \theta} = \frac{1}{Bo}\frac{\partial^2 c}{\partial \chi^2} - \frac{\partial c}{\partial \chi}, \tag{7}$$

which builds on the relative reactor length ($\chi = z/L$) and velocity ($u = L/\tau$) and the definition of the Bodenstein number

$$Bo = Pe_{ax} \cdot \frac{L}{d} = \frac{uL}{D_{ax}} \tag{8}$$

The Bodenstein number characterizes the degree of dispersion [36]. It is directly related to the axial Peclet number (Pe_{ax}) via the ratio of the actual reactor length (L) and the characteristic length (d) describes the intensity of back-mixing in the reactor and serves as a representative to analyze the plug flow behavior of contactors and reactors [45]. It needs to be stressed that this definition is not consistent in literature. The current definition of the right-hand side in Eq. (8) as Bodenstein number is coherent with the textbooks of Emig and Klemm [36], Behr et al. [46] and Darvas et al. [45]. While Hill [47] refers to the term as the Peclet number, Levenspiel [20], argued that the term should neither be referred to as the Peclet, nor the Bodenstein number, and rather referred to it as inverse intensity of axial dispersion or vessel dispersion number. We acknowledge this controversy, recently discussed by Bremer and Turek [48], but keep the definition as Bodenstein number in accordance to the previously mentioned textbooks. As outlined by Levenspiel [20], the reactor approaches ideal plug flow for $\frac{D_{ax}}{uL} \to 0$ ($Bo \to \infty$) and resembles a fully mixed flow, as in a perfect continuously stirred tank reactor, for increasing dispersion when $\frac{D_{ax}}{uL} \to \infty$ ($Bo \to 0$). The analytical solution of the dispersion model in Eq. (9), assuming open boundary conditions and considerable deviations from an ideal plug flow at $Bo \leq 100$ $\left(\frac{D_{ax}}{uL} > 0.01\right)$, is in accordance with Emig and Klemm [36] given by

$$E_{ADM}(\theta) = \sqrt{\frac{Bo}{4\pi \cdot \theta}} exp\left[-\frac{Bo}{4 \cdot \theta}(1-\theta)^2 \right], \; Bo \leq 100 \tag{9}$$

For low axial dispersion with $Bo > 100$ $\left(\frac{D_{ax}}{uL} < 0.01\right)$ this equation can be approximated with sufficient accuracy by the Gaussian normal distribution:

$$E_{ADM}(\theta) = \sqrt{\frac{Bo}{4\pi}} exp\left[-\frac{Bo}{4}(1-\theta)^2 \right], \; Bo > 100 \tag{10}$$

According to heuristics in literature, $Bo > 100$ leads to sufficiently narrow residence time distributions for which the performance in the real reactor can be approximated by an ideal plug flow. With decreasing Bodenstein number, the deviations from an ideal plug flow become stronger, resulting in a wider, more asymmetric distribution.

For modelling the axial dispersion, Taylor [49] and Levenspiel [20] established correlations for the axial dispersion coefficient in laminar and turbulent regime of tubular pipes. In laminar regime ($Re < 2100$), Taylor proposes the following equation of the axial dispersion coefficient in relation to the molecular diffusion coefficient D_m, the hydraulic diameter d_h and the average velocity u [49]:

$$D_{ax} = D_m + \frac{u^2 {d_h}^2}{192 D_m} \tag{11}$$

Levenspiel established a correlation for turbulent regime ($Re > 2100$) in tubular pipes with the axial dispersion coefficient as function of the Reynolds number [20,50]:

$$\frac{D_{ax}}{u d_h} = \frac{3e7}{Re^{2.1}} + \frac{1.35}{Re^{0.125}} \tag{12}$$

While these two models are constrained to simple geometry with limited velocity or length [23,51], micro- reactors are designed with complex channel patterns to enhance heat and mass transfer already at laminar flow conditions. Therefore, Moreau et al. [23] developed an empirical correction for axial dispersion in micro- reactors with the axial dispersion coefficient as function of the Reynolds number, Dean number (De) and aspect ratio (α) of the rectangular cross-section:

$$\frac{D_{ax}}{u d_h} = 4,5 \cdot Re^{1,38} De^{-1,68} \alpha^{-0,53} \tag{13}$$

The Dean number is defined as function of the Reynolds number and the square root of the diameter (d_h) and the curvature radius (R_c) [52]. The aspect ratio a is defined as the ratio of the minimum value of height (h) and width (w) to the maximum value [32].

$$De = Re\sqrt{\frac{d_h}{R_c}} \tag{14}$$

$$\alpha = \frac{\min(h, w)}{\max(h, w)} \tag{15}$$

The correlation from Taylor [49] for the turbulent regime as well as the correlation from Moreau [23] established specifically for micro-reactors are used in this work to establish a correlation for the axial dispersion in the specific type of reactor, which is further described in the subsequent section.

3. Material and methods

After describing the fundamentals for the definition and investigation of the RTD, the specific reactor design, as well as the experimental set-up and the procedures for the analysis of the experimental investigations are described.

3.1. ART plate reactor PR37

The ART plate reactor PR37 from Ehrfeld Mikrotechnik GmbH is designed as an integrated heat exchanger and reactor that pursues process intensification by providing improved heat and mass transfer. The reactor features a modular design that allows the integration of up to 10 reactor plates. The plates are characterized by the meandering, periodically diverging/converging structure of the process channel milled in the upper side, which promotes the formation of secondary flow and intensifies transport processes. The utility channel, used for temperature control, is located below the process channel and contains a turbulator grid to enhance the cross-mixing and therefore the heat transfer. Four different plates (PL37/37–08, PL37/37–3, PL37/37-6 and PL37/37-12) are available with different hold-up volumes but similar geometry and characteristics. The plates only differ in the depth of the process channel and the respective cross-sectional area. Only plate PL37/08 is additionally differing in the width of the channel. This enables a straightforward scale-up of the process, which is even transferable to the ART PR49 plate reactor on a production scale [32]. The modular design of the reactor allows to realize different plate configurations, which are stacked up together in a frame and sealed with tension rods ensuring an even distribution of mechanical stress. The robust reactor design made of stainless steel (SS 316 L) or Hastelloy (C-22) allows a working pressure of up to 20 bar on the process side and up to 10 bar on the utility side, as well as temperatures between −60 and 200 °C. Fig. 2 shows the design of the reactor plates with the meandering, periodically process channel equipped with side ports for temperature control and/or multiple injections.

Furthermore, Table 1 summarizes the geometric dimensions of the four different process plates as well as the nominal volume flow rate and the corresponding hydrodynamic residence times.

3.2. Experimental setup

The RTD of the ART plate reactor PR37 is determined through pulse experiments using UV/VIS spectroscopy as a fast and accurate means for online analysis. For the RTD measurements, flow cells are installed at the inlet and outlet of the reactor which are connected with an Avantes spectrometer (AvaSpec-ULS2048CL-2-RS-EVO). The experimental setup of the RTD studies is further shown in Fig. 3. The RTD is investigated for the three larger plates PL37/3, PL37/6 and PL37/12 using different water-glycerol mixtures and flow rates ranging from 50 - 400 mL/min in

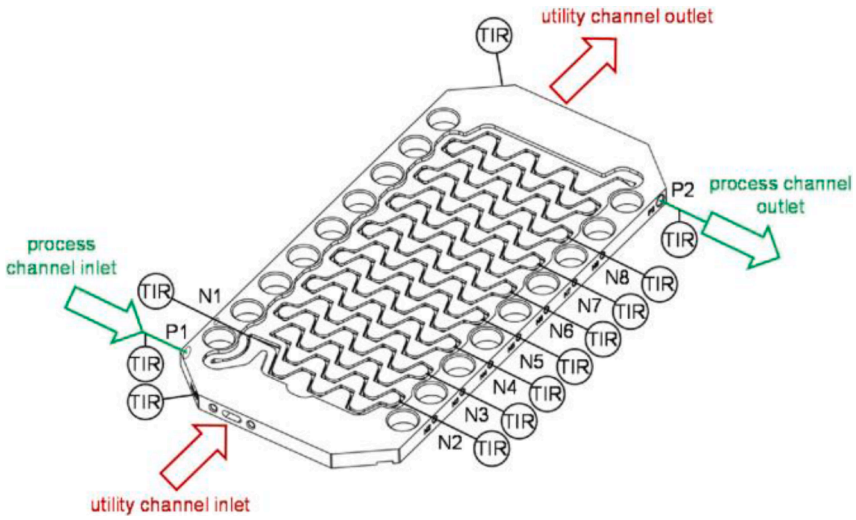

Fig. 2. Structure of a plate displaying the process channel and the ports of the process and utility channel [33].

Table 1
Geometric dimensions of the process channel of the four plate types [19].

	PL37/37/08	PL37/3	PL37/6	PL37/12
Height [mm]	0.8	2.3	4.3	8.3
Width [mm]	1.0–2.0	1.5–3.0	1.5–3.0	1.5–3.0
Cross-sectional area [mm^2]	0.8–1.6	3.4–6.9	6.4–12.9	12.4–24.9
Aspect ratio [-]	0.8–0.4	0.7–1.0	0.4–0.7	0.2–0.4
Hydraulic diameter [mm]	0.9–1.2	1.9–2.7	2.3–3.6	2.6–4.5
Volume [mL]	3.53	13.6	24.9	47.7
Specific surface [$m^2\ m^{-3}$]	3170	1786	1470	1287

order to investigate a wide range of Reynolds numbers ($50 < Re < 1000$). The flow rates are controlled by a gear pump (Reglo-Z Digital, Cole-Parmer Instruments Company LLC.) equipped with a Coriolis mass flow meter (Proline Promass 80, Endress+Hauser Flowtec AG). The considered experimental design space of the three individual plates is summarized in Table 2.

For each individual experiment, a dye (Basic Blue 3) is injected into the flow at the inlet of the reactor using a 100 µL-syringe from Agilent Technologies. During each experiment, repeating injections are performed with an injection volume of about 25 µL. At the inlet and outlet of the reactor, the absorbance maximum ($\lambda_{max} = 654$ nm) of the injected dye is measured with the flow cells in order to determine the dispersion of the dye in the reactor. The absorption signals are detected with a sampling frequency of 20 Hz and recorded via the AvaSpec software. The input and output signals of the injected dye are transformed into RTDs using frequency-discrete deconvolution with the additional use of signal filters. For this purpose, the Fast Fourier Transformation is applied. Subsequently, the result of the axial dispersion model is fitted to the Fourier-transformed RTD data by adjusting the Bodenstein number as sole adjustable parameter. A detailed description of the signal processing is provided in the subsequent section.

3.3. Signal processing

The transformation of the raw data from the spectroscopic measurements into residence time distributions is based on frequency-discrete deconvolution using FFT. Individual absorption intensity data is recorded by means of the Avantes spectrometer as a function of time and wavelength for the input and output signal in the flow cells. These signals are recorded time-discretely with a sampling frequency of 20 Hz and form the basis of the data analysis. The schematic structure of the

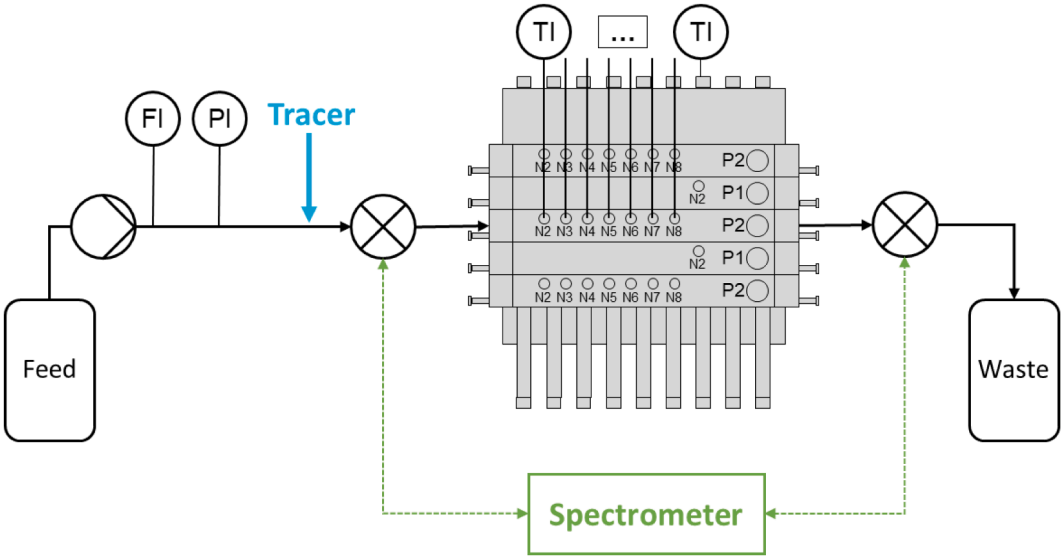

Fig. 3. Experimental setup of the residence time distribution study.

Table 2
Experimental design space of RTD studies in the ART plates PL37/3, PL37/6 and PL37/12.

		PL37/3	PL37/6	PL37/12
Water	Q [mL/min]	50–140	40–200	50–375
	Re [-]	350–1000	200–1000	150–1000
50 % Glycerol	Q [mL/min]	30–125	50–175	100–400
	Re [-]	30–150	30–175	40–175
25 % Glycerol	Q [mL/min]	50–125		
	Re [-]	150–350		

four-step approach for signal processing and analysis using Matlab. is shown in Fig. 4. The first step involves the data preprocessing where the different injection signals are extracted, filtered and normalized. After the data preprocessing, the extracted input and output signals are transferred into the frequency domain using FFT, for the estimation of the frequency-discrete RTD. By application of the inverse FFT, the time-discrete RTD is obtained from the frequency-discrete RTD (cf. Fig. 1). Finally, the estimated RTD is fitted to the ADM by adjusting the Bodenstein number.

The individual steps of the signal processing approach are further illustrated for a selected example. All experiments in the current study are analyzed in analogy to this example. During each experiment, multiple injections were performed at each specified flow rate. Based on the correct match of the injection intervals of each individual experiment the individual input and output signals are extracted and illustrated for the considered example experiment in the ART plate PL37/6 with water at a flow rate of 100 mL/min using four different injections in Fig. 5.

Fig. 5 shows the absorption intensity over time at the wavelength $\lambda_{max} = 654$ nm, corresponding to the absorption maximum of Basic Blue, for the input and output signals. As evident from the illustration, the sampling frequency of about 20 Hz is sufficient to capture all essential features of the signal distribution. The individual injections are further highlighted with different colors to ease identification of the related input and output signals. All input signals show a sharp shape with a high absorption maximum and a very short injection time. Note that all

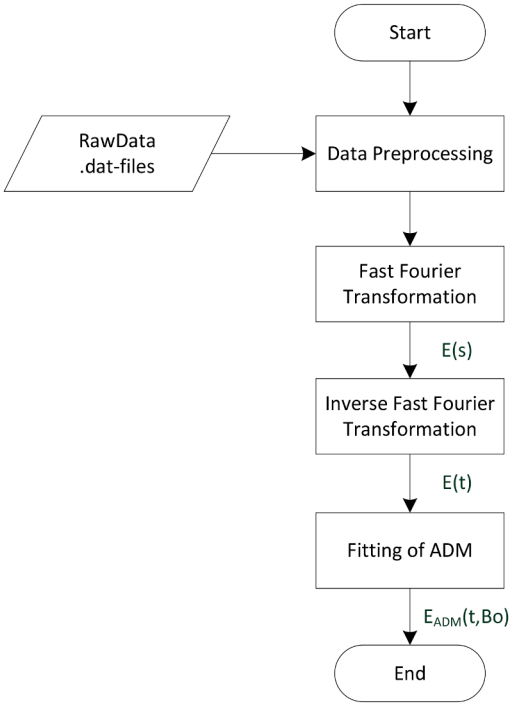

Fig. 4. Schematic structure of signal processing using Matlab.

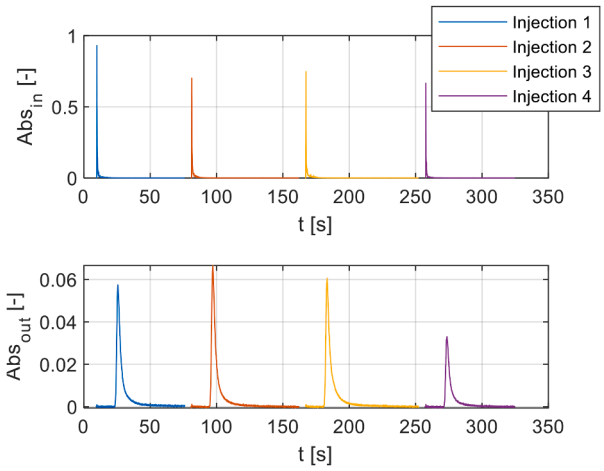

Fig. 5. Input and output signals as function of time for four different injections of ART plate PL37/6 with a flow rate of 100 mL/min.

absorption maxima are below one, which is an essential prerequisite for the linearity between absorption and concentration of the dye [53]. The output signals show a broader distribution with slight tailing to the right with lower absorption maxima.

For further data processing, a moving average filter is used to smooth the output signal in order to improve the signal-to-noise ratio. In contrast to the output signal, filters are not applied for the input signal, because the signal intensity is very short and high resulting in a low data resolution. Therefore, the use of filters is not suitable, otherwise information may be lost [54].

After the filter application, the signals are normalized giving the density functions of the input and output signals. By normalizing the signals, time-discrete functions are created which are directly related to the residence time distribution via the convolution integral from Eq. (4). These provide the basis for further data processing.

The deconvolution of the integral for the determination of the residence time distribution is an inverse problem that cannot be directly solved in the time domain [24]. By transferring the time-discrete signals to the frequency domain, the inverse problem can be transformed into a direct problem. In the frequency domain, a simple multiplication term is obtained from the convolution integral by the following equation:

$$Y(s) = E(s) \cdot X(s) \tag{16}$$

The transformation of the time-discrete signals into the frequency domain is performed using the Fast Fourier Transformation. In the frequency domain, the residence time distribution is determined by simply dividing the frequency-discrete input and output signals according to the following equation:

$$E(s) = \frac{Y(s)}{X(s)} \tag{17}$$

By retransformation using the inverse Fast Fourier Transformation, the time-discrete residence time distribution is derived. The final relation between the residence time distribution and the time-discrete input and output signals is given in Eq. (25):

$$E(t) = \mathfrak{F}^{-1}\{E(s)\} = \mathfrak{F}^{-1}\left\{\frac{\mathfrak{F}\{y(t)\}}{\mathfrak{F}\{x(t)\}}\right\} \tag{18}$$

Fig. 6 shows the residence time distributions for the introduced example in Fig. 5, determined using the described data processing procedure, highlighting the improvements derived by the individual processing steps. As evident from the illustration, the residence time distributions of the four different injections estimated directly from the raw data do overlap but show a generally high noise level (cf. Fig. 6a). The moving-average filter applied on the output signal prior to the FFT

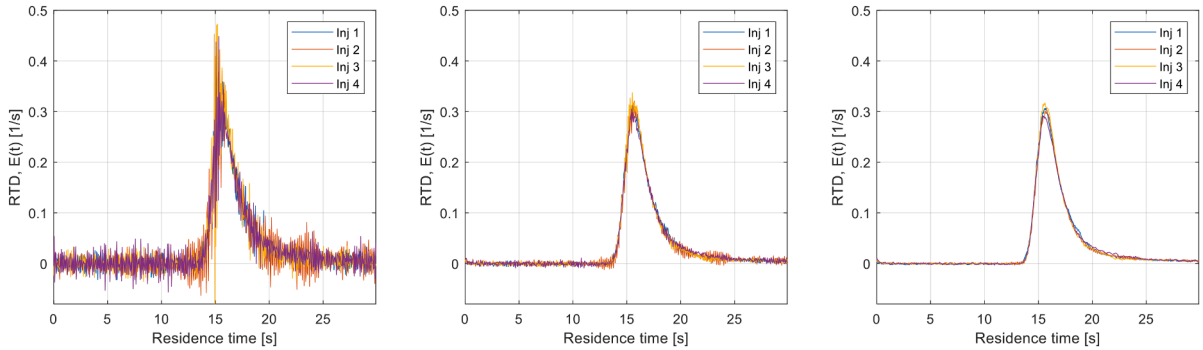

Fig. 6. Residence time distribution extracted from raw data (a), estimated with filtered output signal (b) and smoothed with additional filter on Fourier-transformed RTD (c).

processing lowers the noise level of the RTD significantly (cf. Fig. 6b). By applying an additional moving-average filter on the RTD estimated by IFFT, the noise is further reduced, showing a smooth RTD for all four injections, with a very high agreement (cf. Fig. 6c), confirming the reproducibility of the results of the tracer experiments.

As the final step after deriving the RTD from the experimental data, the axial dispersion model (Eq. 9+10) is fitted to the filtered RTD in order to characterize the deviation from an ideal plug flow. For this purpose, a simple optimization problem that minimizes the sum of squared errors between the experimentally determined RTD and the one resulting from the dispersion model, by varying the Bodenstein number as the sole adjustable parameter:

$$\min_{Bo} \sum_{0}^{t_{max}} [E(t) - E_{ADM}(Bo, t)]^2 \tag{19}$$

The respective optimization problem is solved in Matlab by means of the fminsearch function with the Nelder-Mead simplex algorithm. Fig. 7 shows the result of the regressed axial dispersion model in comparison to the experimentally determined RTD for the given example of the unfiltered and filtered RTD. Comparing the unfiltered and filtered RTD, it is evident that the smoothing filter is slightly truncating the RTD with a deviation of <10 % for E_{max} (t). Despite the slight underprediction of the RTD with the filter, it was decided to treat all signals equally with the same filter, regardless of the signal-to-noise ratio. The axial dispersion model shows the symmetrical form of a Gaussian distribution around the maximum of the RTD, resulting in a good representation of the majority of the RTD. However, there are notable deviations at the left and right side of the RTD, caused by inherent limitation of the one-parametric model to represent asymmetric curves for larger Bodenstein numbers. Besides the tailing, the resulting Bodenstein numbers determined for the RTD from the different injections show only a small deviation with a mean value of Bo = 278 ± 23 indicating a good reproducibility of the RTD. The recognizable effect of tailing typically occurs in millireactors due to the increased influence of frictional forces caused by the small hydraulic diameter [24]. Tailing may also result from tracer adsorption on the reactor material [40] or from inlet effects before entering the reactor, where laminar flow in the inlet tube causes premature dispersion, leading to a so-called “mixing-cup” problem [55]. To better capture the asymmetry of the RTD, alternative empirical models like those proposed by Ham and Platzer [56] or Poulesquen et al. [57] could be applied. Furthermore, since tailing effects of the tracer cannot be excluded, an extended dispersion model named PDE-model (‘Plug flow with axial dispersion and exchange with dead zones’) could be considered for further refinement of the RTD [58]. However, the axial dispersion model provides a sufficient approximation of the residence time distribution in the plate reactor providing valuable insights into the axial dispersion characteristics.

4. Results and discussion

Based on the experimental and analytical approach described in the previous sections, the following two subsections present the results of the RTD measurements and the analysis of the results based on the ADM, providing some insight on the favourable operating window of the ART PR37 reactor. The derivation of specific correlations for the axial

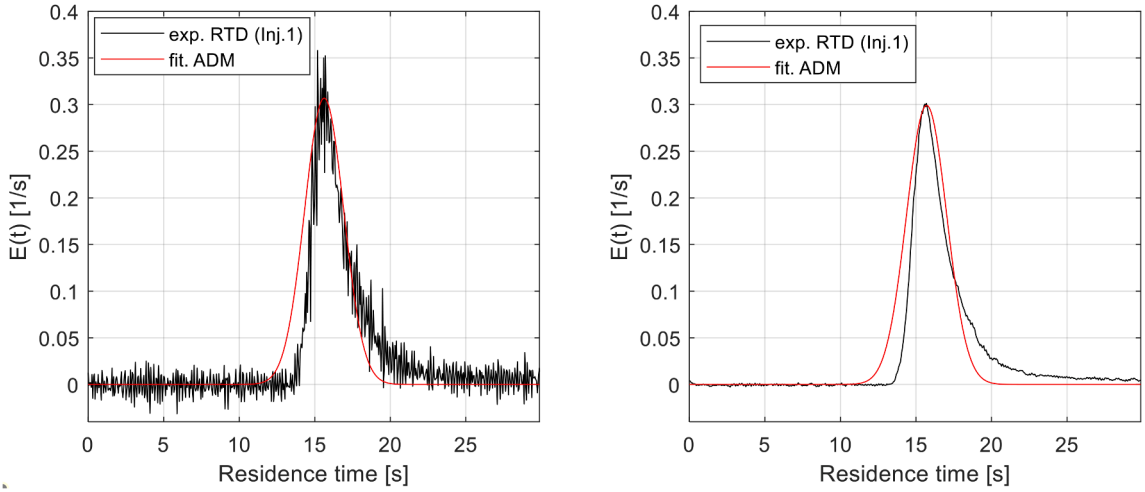

Fig. 7. Residence time distribution and fitted axial dispersion model for injection 1 of plate PL37/6 at a flow rate of 100 mL/min of water for the unfiltered and filtered RTD.

dispersion coefficient further enables a prediction of the RTD for the design and scale-up of the reactor, in order to tailor the design to certain applications.

4.1. RTD analysis of the ART PR37

Based on the described experimental procedure and the data processing approach, the resulting RTDs of the three investigated plates (PL37/3, PL37/6 and PL37/12) are further analyzed at different Reynolds numbers by adjusting the flow rates and water-glycerin compositions according to the experimental conditions stated in Table 2.

Prior to analyzing the overall results of the RTD measurements on the basis of the Bodenstein number as a function of the Reynolds number, some specific features of the ART PR37 are first analyzed on the basis of selected examples. The possible scale-down and scale-up to adjust the operation of the reactor for varying throughput through selection of different plates is first analyzed by comparing the measured RTD's for different plates at approximately constant mean residence times. These are adjusted by the respective flow rate. The RTD of the three different plates is first analyzed at an approximately constant mean residence time of about 10 s considering pure water as solvent. The specific flow rates and the hydrodynamic residence times of the specific plates as well as the mean residence time obtained from the RTD analysis are listed in Table 3. Comparing the hydrodynamic and the mean residence time obtained from the RTD analysis, small deviations are noticeable increasing with decreasing plate volume. The plate PL3 shows the highest deviation with about 5 %, while the deviation for the bigger plates is decreasing. The deviations are caused by inlet effects of the tracer at the reactor periphery due to additional piping between the reactor and the flow cells. With increasing volume, the influence of these inlet effects decreases, and the mean and hydraulic residence times become align.

Fig. 8 shows the unfiltered, filtered and normalized RTD determined from the raw data of the spectroscopic measurements for the three plates with the respective flow rates with four different injections, in accordance to Fig. 6 and the previous description in Section 3.3. All unfiltered RTD's show a noisy signal with overlapping distributions for the four injections. It is interesting to note that the noise level is mitigated with bigger plates. The higher flow rate for the bigger plates mitigates the signal broadening and results in a higher output signal and higher signal-to-noise ratios. By application of the additional smoothing filter, the noise of the signals is considerably reduced providing an improved visibility of the RTD. It becomes even more apparent that the RTD resulting from each individual injection for the plates show a good agreement. Furthermore, the filtered RTD emphasize that an increased flow rate at bigger plates leads to an even narrower and RTD with a more prominent peak, despite the comparable mean residence time. Each of the RTDs can be described with high accuracy on the basis of the ADM after determining the optimal Bodenstein number.

After analyzing the RTD of the three different plates for a comparably similar mean residence time, they are analyzed for a constant flow rate of 100 mL/min. At such constant flow rate, the residence time increase with the individual plate volume as listed in Table 4.

Fig. 9 shows the filtered RTD determined for the different plates and the results of the adjusted ADM for an individual injection. The experimentally estimated RTD is shown in black, while the results of the adjusted ADM are shown in red. In accordance with the volume and cross-sectional area of the plates the PL37/3 has the shortest residence time, with a narrow RTD with a high peak is formed. With increasing plate volume, the residence time is increasing shifting the RTD to the right, but also resulting in a broadening of the RTD. Therefore, the maximum of the RTD is decreasing with residence time and plate volume.

Table 3
Flow rates and residence times of different plates for comparison of constant residence time with water.

	PL37/3	PL37/6	PL37/12
Q [mL/min]	80	140	275
τ [s]	10.2	10.67	10.41
$\bar{t}$ [s]	10.84±0.05	10.98±0.02	10.54±0.04

After showing the effect of the flow rate and residence time on the RTD of the different plates, also the influence of the material properties of the reacting fluid on the RTD is analyzed by comparing three different process media at a constant flow rate of 100 mL/min in the smallest plate PL37/3. Table 5 lists the density (ρ) and viscosity (η) and the resulting Reynolds number for the different fluid mixtures investigated in the specific experiment. By increasing the fraction of glycerol not only the viscosity is increasing significantly, by a factor of 7, but also the Reynolds number is decreased accordingly by the same factor.

Fig. 10 shows the RTD of PL37/3 for water, 25 % glycerol and 50 % glycerol for the first of the four injections. The experimentally measured RTD is again shown in black and the result of the adjusted ADM is shown in red. With higher glycerin fraction and decreasing Reynolds number, friction and wall effects are increasing leading to a more parabolic velocity profile and pronouncing back mixing. With higher Reynolds numbers the increasing turbulence leads to a high degree of radial and axial mixing resulting in a homogenization of the velocity profile and narrow RTD.

The results of all remaining RTD experiments are summarized in the Supplementary Material.

4.2. Application of the axial dispersion model

After analyzing and discussing the RTD of the specific examples the results of the ADM based analysis is discussed on the basis of the full dataset for all three plates. The key parameter for this analysis is the Bodenstein number that is determined from the adjustment of the ADM results in the regression of the experimentally determined RTD. Furthermore, a correlation to describe the axial dispersion in the ART PR37 reactor is established, which is based on the introduced correlations from Levenspiel (Eq. (12)) and Moreau (Eq. (13)). The correlation relies primarily on the basic structure of the correlation for turbulent flow in tubular pipes proposed by Levenspiel [20], extended by an additional factor for the aspect ratio, similar to the correlation for microreactors proposed by Moreau [23]. The resulting correlation of the axial dispersion coefficient for the ART reactor plates established within this work

$$\frac{D_{ax}}{ud_h} = \frac{1.5e3}{\alpha \cdot Re^{1.43}} + \frac{\alpha \cdot 42.1}{Re^{0.255}}, \tag{20}$$

defines the dispersion coefficient as function of the Reynolds number and the aspect ratio with four additional fitting parameters. The correlation consists of two terms, each including a constant, an exponential factor for the Reynolds number and the aspect ratio. Table 6 lists the correlation parameters and their corresponding σ-confidence intervals (CIp).

In order to analyze the results of the ADM for the totality of the experiments, Fig. 11 plots the Bodenstein number in relation to the Reynolds number for the three different plates. The individual data points represent the mean Bodenstein number, while the error bars indicate the standard deviation based on four injections per experiment. Additionally, the correlation of the axial dispersion fitted to the experimental data is shown in dashed lines, which is introduced in Eq. (20).

Fig. 11 shows a general trend that reflects an increase of the Bodenstein number with increasing Reynolds numbers for all three plate. Obviously, this dependence is not linear and the slope of the curves of the fitted correlations decreases with an increase in the Reynlods number. The relationship between the two dimensionless numbers can be divided into two sections separated at around $Re = 200$, at which the

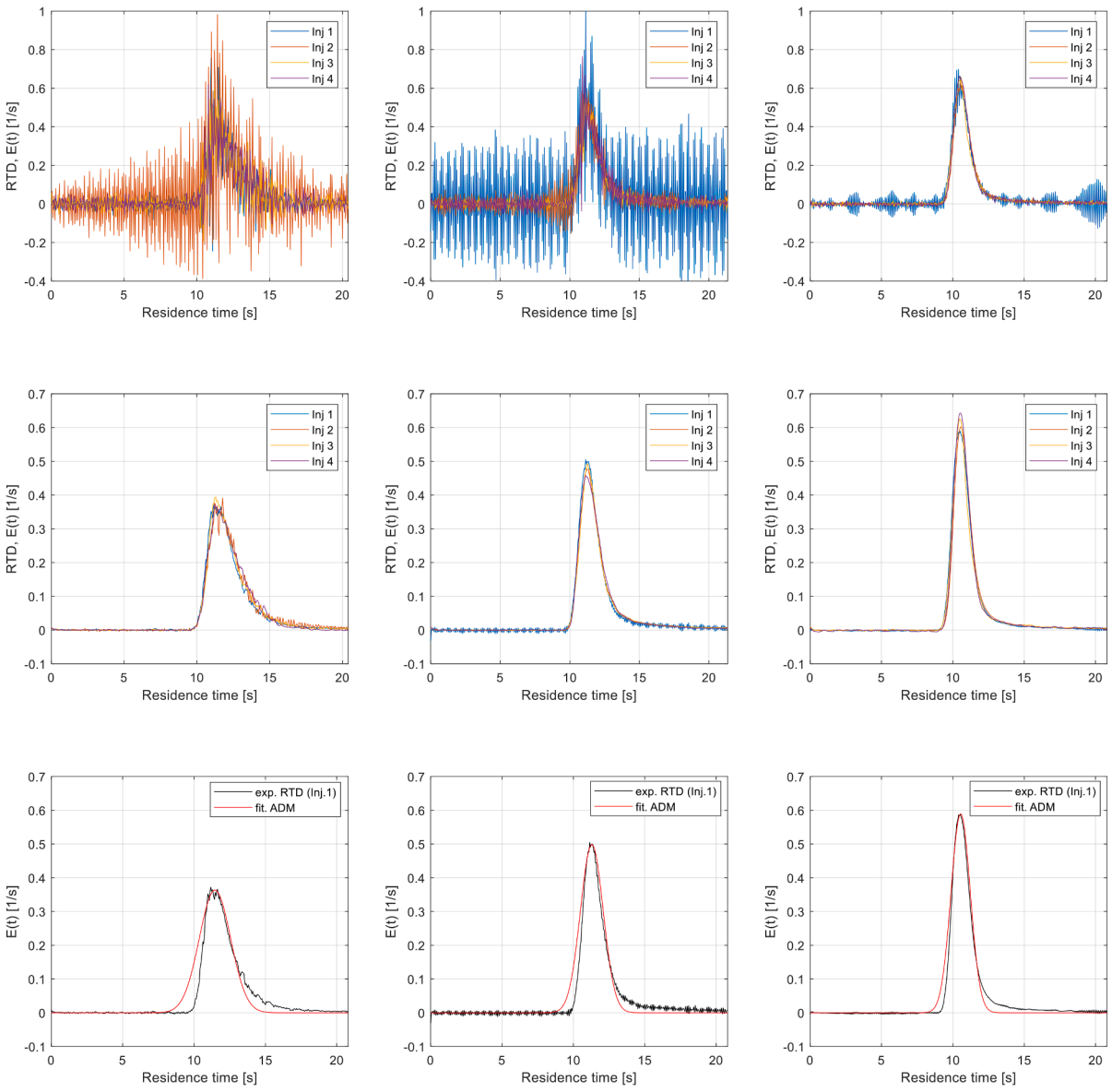

Fig. 8. Results of the RTD experiments with approximately constant mean residence time according to the flow rates in Table 3 for the plates PL37/3 (left), PL37/6 (center) and PL37/12 (right), showing the non-filtered RTD data (top), the filtered RTD (center) and the results of the ADM model fitted to the filtered data (bottom).

Table 4
Residence times of specific plates for comparison of constant flow rate of 100 mL/min with water.

	PL37/3	PL37/6	PL37/12
τ [s]	8.16	14.94	28.62
$\bar{t}$ [s]	8.67±0.04	15.32±0.05	28.29±0.23

Bodenstein number of the three plates intersect with an approximately equivalent Bodenstein number of around 200.

For $Re > 200$, the slope of the correlation curves for the Bodenstein number further depart for the different plates, with the steepest slope for the biggest plate, PL37/12, which reaches a Bodenstein number of around 650 at the highest investigated Reynolds number of about 1000. In contrast to that, the increase of the Bodenstein number is lowest for the smallest plate, PL37/3, reaching a maximum Bodenstein number of around 325 at similar Reynolds numbers. The medium-sized plate, PL37/6, has a moderate slope compared to the other plates, with a maximum Bodenstein number roughly between the other two. While these differences are important for the design and scale-up of the reactor it is important to highlight, that all plates exceed the critical Bodenstein number of 100 already for much lower Reynolds numbers, showcasing that the ART PR37 approaches ideal plug flow for a wide range of operating conditions.

For $Re < 200$ the trend shifts slowly, whereas the Bodenstein number of the smallest plate initially increases the fastest and exceeds the critical Bodenstein number of 100 already for Reynolds numbers of about $Re = 60$. For the largest plate, PL37/12, the slope is initially the lowest exceeding the critical Bodenstein number of 100 at Reynolds numbers of about $Re = 130$. The medium-sized plate, PL37/6, shows a moderate increase, but also exceeds the critical value of Bo =100 with an approximately linear slope at $Re = 90$.

While $Re < 200$ appears to indicate a transition regime to laminar flow, for $Re > 200$ the convection forces are predominant over the frictional forces. With an increasing Reynolds number, the proportion of convection forces increases, which reduces axial dispersion. Additionally, the periodic deflections in the channels lead to an intensified formation of secondary flows, resulting in an enhanced cross-mixing which in return reduces axial dispersion. Comparing the different plates, the

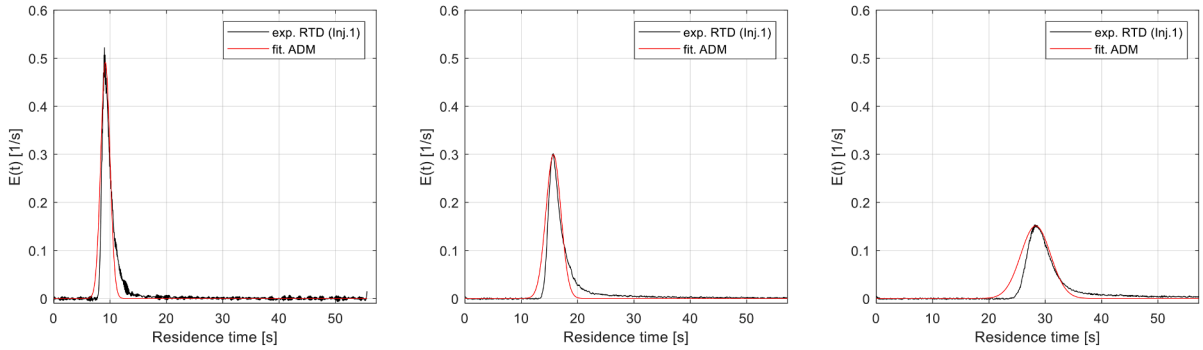

Fig. 9. Residence time distribution from the filtered experimental data and the adjusted axial dispersion model for a constant water flow rate of 100 mL/min, for an individual injection for plate PL37/3 (left), PL37/6 (center) and PL37/12 (right).

Table 5
Reynolds number of PL37/3 for water, 25 % glycerol and 50 % glycerol constant flow rate of 100 mL/min.

	water	25 % glycerol	50 % glycerol
ρ [kg/m^3]	1000	1065	1130
η [Pa s]	1e-3	2.58e-3	7.17e-3
Re [-]	700	272	97

bigger plates result in higher Bodenstein numbers and hence a lower dispersion at comparable Reynolds numbers. This effect is likely caused by the lower cross-section aspect ratio of the bigger plates, which leads to a low ratio of maximum velocity u_{max} to the mean velocity u_m creating a more evenly distributed velocity profile and therefore reducing the axial dispersion. Similar effects have been reported for a laminar flow in straight microchannels [25,59]. An increasing aspect ratio results in a higher ratio of u_{max}/u_m and hence a higher axial dispersion. In this region, the reduction of the Bodenstein number relative to the maximum Bodenstein number increases with increasing plate size until $Re = 200$, where the Bodenstein number of the plates intersect. The steeper gradient of the correlations for the Bodenstein over Reynolds number for low aspect ratios might therefore be explained by the bigger difference between the laminar and turbulent velocity profiles in more rectangular channels.

Moving from higher to lower Reynolds numbers it can be concluded that the small plate can maintain an ideal plug flow characteristic longer than the bigger plates in the transition range $Re < 200$, for which a parabolic velocity profile is developing. As convection forces decrease, cross-mixing, caused by tangential forces at the channel's deflections, becomes the main driver for the reduction of axial dispersion. In case of high aspect ratios, cross-mixing has relatively a bigger impact on the total cross-section and the velocity profile which may be the reason for the reduced axial dispersion [23]. In comparison to that, low aspect ratios produce less effective cross-mixing which is in laminar regime the main factor for reduction of axial dispersion. This results in an increasing axial dispersion for the bigger plates with low aspect ratio and allows the smaller plate to maintain an ideal plug flow characteristic even at lower Reynolds numbers.

Fig. 12 compares the results of the Bodenstein number estimated through the ADM analysis from the experiments and predicted values estimated by the introduced correlation in Eq. (20) in a parity plot. The results of the predictions on the basis of the correlation are generally in good agreement with the analytically derived Bodenstein number form the experimentally determined RTD. The majority of the data are in the range of 25 % relative error, with even higher accuracy for higher Bodenstein numbers, indicating a very good accuracy of the correlation. However, at low Bodenstein numbers, the correlation should be used with caution due the higher relative uncertainties and the lack of data for viscous media.

Additionally, Fig. 13 shows a comparison of the actual values for the axial dispersion coefficient estimated from the Bodenstein number of the experiments and those calculated by the correlation, plotted on a logarithmic scale. Equivalent to Fig. 12, the experimental and the modeled values show an excellent agreement, with somewhat larger deviations for higher axial dispersion coefficients. Overall, it is evident that the ART PR37 reactor provides low axial dispersion with coefficients between $0.001\ m^2/s < D_{ax} < 0.01\ m^2/s$ across the full spectra of the

Table 6
Correlation parameters and corresponding confidence intervals.

	$c_1 \pm$ CIp [-]	$c_2 \pm$ CIp [-]	$c_3 \pm$ CIp [-]	$c_4 \pm$ CIp [-]
Parameter	1488 ± 40.2 %	42.1 ± 23.7 %	1.433 ± 4.8 %	0.255 ± 14.5 %

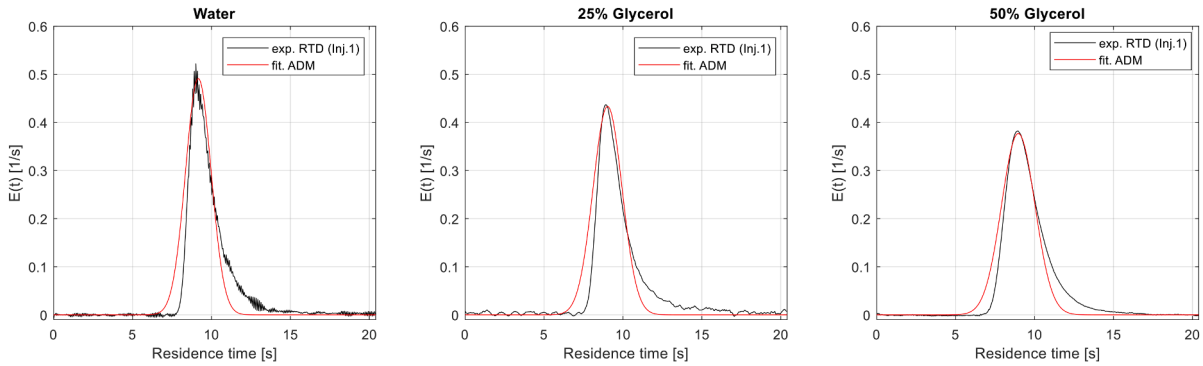

Fig. 10. Residence time distribution and fitted axial dispersion model at constant flow rate of 100 mL/min for injection 1 of PL37/3 with water, 25 % glycerol and 50 % glycerol.

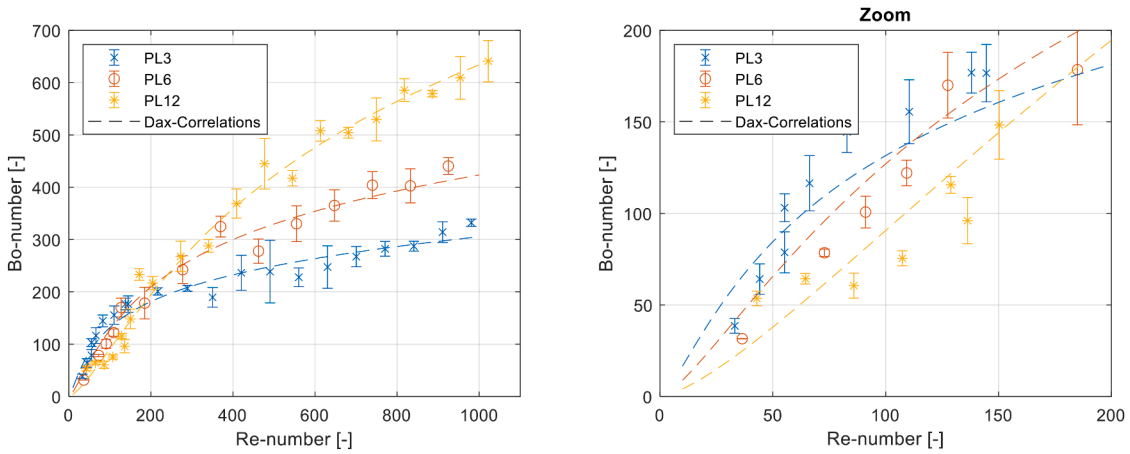

Fig. 11. Bodenstein number as a function of the Reynolds number for the ART plates PL37/3, PL37/6 and PL37/12 in the full range of investigated Reynolds numbers (left) and enlarged for the region of low Reynolds numbers (right).

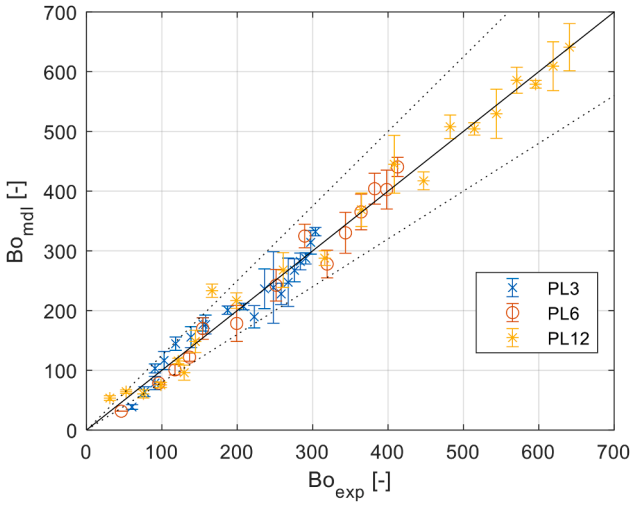

Fig. 12. Comparison of Bodenstein number estimated by experiments and predicted by the correlation given by Eq. (26). Dashed lines correspond to 25 % of relative error.

investigated wide process window. Again, the deviations between correlation and experimental data increase at high dispersion coefficients, indicating that the correlation should be used cautiously at high dispersion outside the identified plug flow regime.

Finally, the macromixing characteristics of the ART PR37 reactor are compared with those of circular pipes as described by the two correlations for the laminar and turbulent regime derived by Taylor [49] and Levenspiel [20]. For this purpose, the Bodenstein numbers derived from the ADM analysis of the experimental data and the ones calculated with the correlations in Eq. (11) and (12) are illustrated in Fig. 14 as a function of the Reynolds number, with the parameters described in the Figure caption. Additionally, the correlation of Moreau, applied for the parameters of the mean plate (PL6), is shown for comparison. The diagram demonstrates that the ART reactor exceeds the laminar flow regime at low Reynolds number, exhibiting similar macromixing characteristics as experienced at turbulent flow in the circular pipes at significantly higher Reynolds numbers. This results from the meandering, periodically diverging/converging structure of the process channels inducing secondary flow which intensifies cross-mixing and reduces axial dispersion. Compared to Moreau's correlation, which follows a fixed power law relationship between the Bodenstein and the Reynolds number–evident from its linear trend on the log-log scale – it

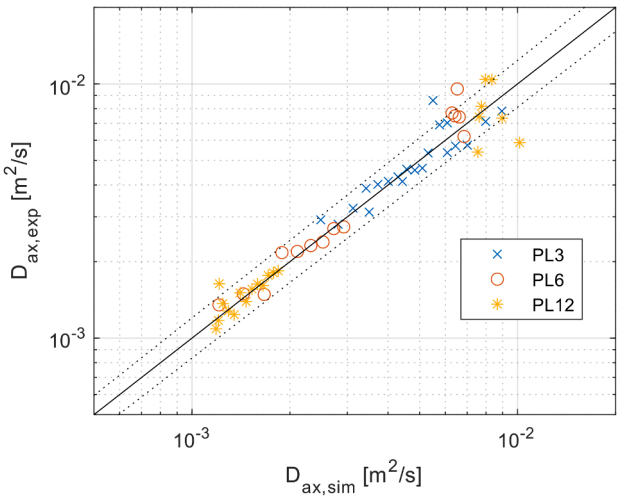

Fig. 13. Logarithmic comparison of axial dispersion coefficients estimated by experiments and calculated by the correlation given by Eq. (26). Dashed lines correspond to 25 % of relative error.

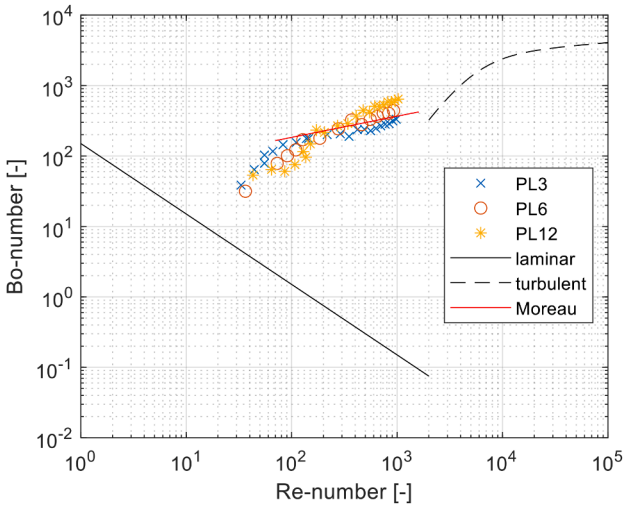

Fig. 14. Bodenstein number as function of Reynolds number for experimental results of PL37/3, PL37/6 and PL37/12 and for the correlations of laminar and turbulent flow regime as well as the correlation of Moreau et al. (L = 3 m, d_h = 2.3 mm, D_m = 6e-10 m^2/s, ν=1e-3 m^2/s).

only aligns with the results for the mean plate (PL6) at $Re > 200$, indicating the transition to turbulent regime, but shows significant deviations at lower Reynolds numbers. For the other plates, the deviations are even higher, likely because their hydraulic diameter and aspect ratio fall outside the calibration range of the correlation (d_h(PL3) < 2 mm, α(PL12) < 0.25). In contrast, the turbulent correlation, whose basic structure was used for the established correlation (Eq. (20)), demonstrates better adaptability across the entire range of Reynolds numbers, making it more suitable for describing the RTD characteristics of the ART reactor. Most importantly, the structured design of the ART plates enables an early transition out of laminar flow regime, resulting in plug flow characteristics.

5. Summary and conclusion

This work performed a detailed analysis of the residence time distribution (RTD) of the millistructured ART plate reactor PR37 on the basis of pulse experiments using UV/VIS spectroscopy. The RTD of the ART reactor has been investigated for the three plates PL37/3, PL37/6 and PL37/12, which provide different volume and cross-sectional area. Furthermore, a broad process window with Reynolds numbers between $30 < Re < 1000$ has been analyzed, changing not only the flowrates, but also the processed fluid and its properties. Based on a robust method for signal processing implemented in Matlab, the time-discrete input and output signals of the injected dye were transformed into RTD based on frequency-discrete deconvolution using Fast Fourier Transformation. In order to analyze the Fourier-transformed RTD, the axial dispersion model (ADM) was applied with the Bodenstein number as the key parameter to describe the deviation from an ideal plug flow. The ADM was adjusted to the estimated RTD by minimizing the sum of square error, adjusting the Bodenstein number as single variable.

One of the key findings is that the ART PR37 exceeds Bodenstein numbers of 100, indicating an accurate approximation of ideal plug flow, for all of the three investigated plates (PL37/3, PL37/6 and PL37/12) at remarkably low Reynolds numbers. The smallest plate, PL37/3, exceeds the critical Bodenstein number of Bo = 100 already at a Reynolds number of only $Re = 60$. The two bigger plates surpass Bo = 100 at $Re = 90$ for the medium-sized plate, PL37/6, and $Re = 130$ for the biggest plate, PL37/12. Based on the results, two flow regimes are identified with a transition at approximately $Re = 200$. The fast transition to an ideal plug flow characteristic results from the meandering, periodically diverging/converging process channels which promote the formation of secondary flow and lead to an intensified cross-mixing reducing the axial dispersion. The reactor is therefore an excellent example for the process intensification by means of structuring.

Based on the experimental results and analysis, a correlation for the axial dispersion coefficient was established which accurately resembles the whole set of experimental data by adjusting just four empirical parameters. The correlation builds on the correlation for the turbulent regime in tubular pipes as described by Levenspiel [20] and enables further prediction of the axial dispersion coefficient as function of the Reynolds number, further considering an extension for the aspect ratio. The current results demonstrate that this correlation is applicable in a wide process window for different reactor plates of the ART PR37 from Ehrfeld Mikrotechnik GmbH. It can therefore be used to evaluate the applicability and support the design and scale-up of the reactor. At low Reynolds numbers for viscous fluids, the correlation should nevertheless be used with caution due to the increasing uncertainty and limited data.

In summary, the ART reactor offers low axial dispersion with dispersion coefficients in the range of $0.001\ m^2/s < D_{ax} < 0.01\ m^2/s$, ensuring a good approximation of ideal plug flow for a wide range of operating conditions. Most importantly the currently derived correlation allows to evaluate if ideal plug flow can be assumed and can be directly integrated in the ADM in case this is not feasible. Alongside with the excellent heat transfer [33] and the fast micromixing [34] that have been demonstrated in preceding work, the ART PR37 reactor provides well-defined process conditions which allow nearly ideal operation over a wide range of process conditions and the exploration of new process windows to exploit intrinsic reaction kinetics, which are not constrained by limitations of heat transfer, dispersion or mixing. Future work will aim at exploitation of these characteristics and the proving the excellent suitability of the reactor for fast and mixing-sensitive, highly exothermic reactions as well as complex reaction networks with instable intermediates and undesired by-products.

CRediT authorship contribution statement

Lucas Schaare: Writing – original draft, Validation, Software, Methodology, Investigation, Conceptualization. **Alexander Rave:** Writing – review & editing, Validation, Methodology. **Rafael Kuwertz:** Writing – review & editing, Project administration. **Georg Fieg:** Writing – review & editing, Project administration. **Mirko Skiborowski:** Writing – review & editing, Project administration, Funding acquisition.

Declaration of competing interest

The authors declare that they have no known competing financial interests or personal relationships that could have appeared to influence the work reported in this paper.

Acknowledgements

LS, AR, GF and MS greatly appreciate and acknowledge the provision of the ART PR37 reactor and further parts of the experimental equipment by Ehrfeld Mikrotechnik. LS, RK and MS further acknowledge the financial support from German Federal Ministry for Economic Affairs and Energy through ZIM program (Zentrales Innovationsprogramm Mittelstand, project number: KK5595001BR3).

Supplementary materials

Supplementary material associated with this article can be found, in the online version, at doi:10.1016/j.cep.2025.110295.

Data availability

Data will be made available on request.

References

[1] P. Gabrielli, L. Rosa, M. Gazzani, R. Meys, A. Bardow, M. Mazzotti, G. Sansavini, Net-zero emissions chemical industry in a world of limited resources, One Earth 6 (2023) 682–704, https://doi.org/10.1016/j.oneear.2023.05.006.
[2] A. Stankiewicz, T. van Gerven, G. Stefanidis, The Fundamentals of Process Intensification, 1st. Auflage, Wiley-VCH, Weinheim, 2019.
[3] V. Hessel, I.V. Gürsel, Q. Wang, T. Noël, J. Lang, Potenzialanalyse von milli- und mikroprozesstechniken für die verkürzung von prozessentwicklungszeiten - chemie und prozessdesign als intensivierungsfelder, Chem. Ingen. Tech. 84 (2012) 660–684, https://doi.org/10.1002/cite.201200007.
[4] De Gruyter (Ed.), Flow Chemistry, 2014. Berlin.
[5] V. Hessel, Novel process windows - gate to maximizing process intensification via flow chemistry, Chem. Eng. Technol. 32 (2009) 1655–1681, https://doi.org/10.1002/ceat.200900474.
[6] K. Jähnisch, V. Hessel, H. Löwe, M. Baerns, Chemistry in microstructured reactors, Angew. Chem. Int. Ed. Engl. 43 (2004) 406–446, https://doi.org/10.1002/anie.200300577.
[7] F. Schönfeld, V. Hessel, C. Hofmann, An optimised split-and-recombine micro-mixer with uniform chaotic mixing, Lab. Chip. 4 (2004) 65–69, https://doi.org/10.1039/B310802C.
[8] Z. Anxionnaz-Minvielle, M. Cabassud, C. Gourdon, P. Tochon, Influence of the meandering channel geometry on the thermo-hydraulic performances of an intensified heat exchanger/reactor, Chem. Eng. Process. 73 (2013) 67–80, https://doi.org/10.1016/j.cep.2013.06.012.
[9] M. Moreau, N. Di Miceli Raimondi, N. Le Sauze, M. Cabassud, C. Gourdon, Pressure drop and axial dispersion in industrial millistructured heat exchange reactors, Chem. Eng. Process. 95 (2015) 54–62, https://doi.org/10.1016/j.cep.2015.05.009.

[10] T. van Gerven, A. Stankiewicz, Structure, energy, synergy, time—the fundamentals of process intensification, Ind. Eng. Chem. Res. 48 (2009) 2465–2474, https://doi.org/10.1021/ie801501y.

[11] D. Cantillo, C.O. Kappe, Halogenation of organic compounds using continuous flow and microreactor technology, React. Chem. Eng. 2 (2017) 7–19, https://doi.org/10.1039/C6RE00186F.

[12] J.R. Bourne, Mixing and the selectivity of chemical reactions, Org. Process. Res. Dev. 7 (2003) 471–508, https://doi.org/10.1021/op020074q.

[13] M. Kashid, A. Renken, L. Kiwi-Minsker, Microstructured Devices For Chemical Processing, Wiley-VCH, Weinheim, Germany, 2015.

[14] Z. Dong, Z. Wen, F. Zhao, S. Kuhn, T. Noël, Scale-up of micro- and milli-reactors: an overview of strategies, design principles and applications, Chem. Eng. Sci. X 10 (2021) 100097, https://doi.org/10.1016/j.cesx.2021.100097.

[15] Corning Advances Flow Reactor Technology For Industrial Chemical Production, 2024. https://www.corning.com/worldwide/en/about-us/news-events/corning-advances-flow-reactor-technology-for-industrial-chemical-production.html (Accessed 9 October 2024).

[16] B. Schäfer, J. Sauer, Trends der chemischen Prozessindustrie, Chem. Ingen. Tech. 92 (2020) 183–191, https://doi.org/10.1002/cite.201900178.

[17] C. Holtze, R. Boehling, Batch or flow chemistry? – A current industrial opinion on process selection, Curr. Opin. Chem. Eng. 36 (2022) 100798, https://doi.org/10.1016/j.coche.2022.100798.

[18] H.S. Fogler, M.N. Gürmen, Elements of Chemical Reaction Engineering, 4th ed., Prentice Hall PTR/Pearson Education Internat, Upper Saddle River, NJ, 2006.

[19] S.A. May, M.D. Johnson, T.M. Braden, J.R. Calvin, B.D. Haeberle, A.R. Jines, R. D. Miller, E.F. Plocharczyk, G.A. Rener, R.N. Richey, C.R. Schmid, R.K. Vaid, H. Yu, Rapid development and scale-up of a 1 H -4-substituted imidazole intermediate enabled by chemistry in continuous plug flow reactors, Org. Process. Res. Dev. 16 (2012) 982–1002, https://doi.org/10.1021/op200351g.

[20] O. Levenspiel, Chemical Reaction Engineering, 3rd ed., Wiley, Hoboken, NJ, 1999.

[21] M.H. Reis, T.P. Varner, F.A. Leibfarth, The influence of residence time distribution on continuous-flow polymerization, Macromolecules. 52 (2019) 3551–3557, https://doi.org/10.1021/acs.macromol.9b00454.

[22] A. Hopley, B.J. Doyle, D.M. Roberge, A. Macchi, Residence time distribution in coil and plate micro-reactors, Chem. Eng. Sci. 207 (2019) 181–193, https://doi.org/10.1016/j.ces.2019.06.016.

[23] M. Moreau, N. Di Miceli Raimondi, N. Le Sauze, C. Gourdon, M. Cabassud, A new numerical method for axial dispersion characterization in microreactors, Chem. Eng. Sci. 168 (2017) 178–188, https://doi.org/10.1016/j.ces.2017.04.040.

[24] D. Bošković, S. Loebbecke, G.A. Gross, J.M. Koehler, Residence time distribution studies in microfluidic mixing structures, Chem. Eng. Technol. 34 (2011) 361–370, https://doi.org/10.1002/ceat.201000352.

[25] M. Wörner, Approximate residence time distribution of fully develop laminar flow in a straight rectangular channel, Chem. Eng. Sci. 65 (2010) 3499–3507, https://doi.org/10.1016/j.ces.2010.02.047.

[26] P. Bouvier, C. André, S. Russeil, Effect of Reynolds number on laminar mixing in an annular tube combining two crossed secondary flows, Chem. Eng. Technol. 42 (2019) 100–108, https://doi.org/10.1002/ceat.201800134.

[27] S.K. Kurt, M.G. Gelhausen, N. Kockmann, Axial dispersion and heat transfer in a milli/microstructured coiled flow inverter for narrow residence time distribution at laminar flow, Chem. Eng. Technol. 38 (2015) 1122–1130, https://doi.org/10.1002/ceat.201400515.

[28] S. Klutz, S.K. Kurt, M. Lobedann, N. Kockmann, Narrow residence time distribution in tubular reactor concept for Reynolds number range of 10–100, Chem. Eng. Res. Des. 95 (2015) 22–33, https://doi.org/10.1016/j.cherd.2015.01.003.

[29] S.R.L. Gobert, S. Kuhn, L. Braeken, L.C.J. Thomassen, Characterization of milli- and microflow reactors: mixing efficiency and residence time distribution, Org. Process. Res. Dev. 21 (2017) 531–542, https://doi.org/10.1021/acs.oprd.6b00359.

[30] É.S. Siguemoto, L. Leite Reche, J.A.W. Gut, M.S.A. Palma, Residence time distribution of a capillary microreactor used for pharmaceutical synthesis, Chem. Eng. Technol. 43 (2020) 429–435, https://doi.org/10.1002/ceat.201900478.

[31] M.S. Khan, H.S. Deore, A.A. Kulkarni, Hydrodynamics, residence time distribution, and mass transfer in spiral coils in series, Ind. Eng. Chem. Res. 62 (2023) 21822–21834, https://doi.org/10.1021/acs.iecr.3c02859.

[32] A. Rave, R. Kuwertz, G. Fieg, J. Heck, Characterization of a modular, scalable millistructured plate reactor, Chem. Ingen. Tech. 91 (2019) 602–606, https://doi.org/10.1002/cite.201800203.

[33] A. Rave, R. Kuwertz, G. Fieg, J. Heck, Modeling and experimental investigation of the spatial heat transfer in a plate reactor with meandering millichannels, Chem. Eng. Process. 150 (2020) 107860, https://doi.org/10.1016/j.cep.2020.107860.

[34] A. Rave, L. Schaare, G. Fieg, Investigation of micromixing in the ART plate reactor PR37 using the acetal cleavage method and different mixing models, Chem. Eng. Process. 181 (2022) 109134, https://doi.org/10.1016/j.cep.2022.109134.

[35] W. Reschetilowski (Ed.), Handbuch Chemische Reaktoren, Springer Berlin Heidelberg, Berlin, Heidelberg, 2020.

[36] G. Emig, E. Klemm, Chemische Reaktionstechnik, Springer Vieweg, Berlin, Heidelberg, 2017 sixth., neu bearbeitete Auflage.

[37] P.V. Danckwerts, Continuous flow systems, Chem. Eng. Sci. 2 (1953) 1–13, https://doi.org/10.1016/0009-2509(53)80001-1.

[38] S. Lohse, Experimentelle Bestimmung der Verweilzeitverteilung in Mikroreaktoren, Der Andere Verl., Tönning, Lübeck, Marburg, 2010.

[39] K. Hertwig, L. Martens, C. Hamel, Chemische Verfahrenstechnik: Berechnung, Auslegung, und Betrieb chemischer Reaktoren, third. Auflage, De Gruyter, Berlin, Boston, 2018.

[40] D. Bošković, Experimentelle bestimmung und modellierung des verweilzeitverhaltens mikrofluidischer strukturen. Dissertation, Fraunhofer-Verl., Stuttgart, 2011.

[41] F. Pichler, Matematische Systemtheorie, De Gruyter, 1975.

[42] P. Rojahn, V. Hessel, K.D. Nigam, F. Schael, Applicability of the axial dispersion model to coiled flow inverters containing single liquid phase and segmented liquid-liquid flows, Chem. Eng. Sci. 182 (2018) 77–92, https://doi.org/10.1016/j.ces.2018.02.031.

[43] A. Fick, Ueber Diffusion, Ann. Phys. 170 (1855) 59–86, https://doi.org/10.1002/andp.18551700105.

[44] M. Baerns, H. Hofmann, A. Renken, Lehrbuch Der Technischen Chemie, 1999 third., durchges. Aufl., Thieme, Stuttgart.

[45] F. Darvas, G. Dormán, V. Hessel, S.V. Ley, Flow Chemistry, 2nd ed., De Gruyter, Berlin, Boston, 2021.

[46] A. Behr, D.W. Agar, J. Jörissen, A.J. Vorholt, Einführung in Die Technische Chemie, second. Aufl. Twentiethsixteenth, Springer Berlin Heidelberg, Berlin, Heidelberg, 2016.

[47] C.G. Hill, T.W. Root, Introduction to Chemical Engineering Kinetics and Reactor Design, 2nd ed., Wiley, Hoboken, New Jersey, 2014.

[48] J. Bremer, T. Turek, From bodenstein to péclet – dimensionless numbers for axial dispersion in chemical reactors, Chem. Ingen. Tech. (2024), https://doi.org/10.1002/cite.202400102 cite.202400102.

[49] Taylor, Dispersion of soluble matter in solvent flowing slowly through a tube, Proc. R. Soc. Lond. A 219 (1953) 186–203, https://doi.org/10.1098/rspa.1953.0139.

[50] P. Trambouze, J.-P. Euzen, Chemical reactors: From design to Operation, New ed., Editions Technip, Paris, 2004.

[51] K.D. Nagy, B. Shen, T.F. Jamison, K.F. Jensen, Mixing and dispersion in small-scale flow systems, Org. Process. Res. Dev. 16 (2012) 976–981, https://doi.org/10.1021/op200349f.

[52] W.R. Dean, Fluid motion in a curved channel, Proc. R. Soc. Lond. A 121 (1928) 402–420, https://doi.org/10.1098/rspa.1928.0205.

[53] T.G. Mayerhöfer, J. Popp, Beer's law - why absorbance depends (almost) linearly on concentration, Chemphyschem. 20 (2019) 511–515, https://doi.org/10.1002/cphc.201801073.

[54] A.V. Oppenheim, R.W. Schafer, Discrete-time signal processing. Pearson New international Edition, 3rd ed., Pearson, Harlow, 2014.

[55] O. Levenspiel, J. Turner, The interpretation of residence-time experiments, Chem. Eng. Sci. 25 (1970) 1605–1609, https://doi.org/10.1016/0009-2509(70)85083-7.

[56] J.-H. Ham, B. Platzer, Semi-empirical equations for the residence time distributions in disperse systems - Part 1: continuous phase, Chem. Eng. Technol. 27 (2004) 1172–1178, https://doi.org/10.1002/ceat.200407038.

[57] A. Poulesquen, B. Vergnes, P. Cassagnau, A. Michel, O.S. Carneiro, J.A. Covas, A study of residence time distribution in co-rotating twin-screw extruders. Part II: experimental validation, Polym. Eng. Sci. 43 (2003) 1849–1862, https://doi.org/10.1002/pen.10157.

[58] C. Castelain, D. Berger, P. Legentilhomme, A. Mokrani, H. Peerhossaini, Experimental and numerical characterisation of mixing in a steady spatially chaotic flow by means of residence time distribution measurements, Int. J. Heat. Mass Transf. 43 (2000) 3687–3700, https://doi.org/10.1016/S0017-9310(99)00363-4.

[59] J. Aubin, L. Prat, C. Xuereb, C. Gourdon, Effect of microchannel aspect ratio on residence time distributions and the axial dispersion coefficient, Chem. Eng. Process. 48 (2009) 554–559, https://doi.org/10.1016/j.cep.2008.08.004.